ROYAL SOCIETY
OF CHEMISTRY

Check for updates

Unrivaled accuracy in measuring rotational transitions of greenhouse gases: THz CRDS of CF$_4$†

Fabien Simon, [ID] [a] Arnaud Cuisset, [ID] *[a] Coralie Elmaleh, [ID] [a] Francis Hindle, [ID] [a] Gaël Mouret, [ID] [a] Michaël Rey, [ID] [b] Cyril Richard [ID] [c] and Vincent Boudon [ID] [c]

Tetrafluoromethane CF$_4$ is the most abundant perfluorocarbon in the atmosphere, where it is designated as PFC-14. This greenhouse gas is very stable, has an atmospheric lifetime of 50 000 years, and a high greenhouse warming potential 6500 times that of CO$_2$. Over the last 15 years, its atmospheric concentration has increased at a rate of 0.8 ppt per year. The accurate quantification of CF$_4$ is key to understanding the contribution of its emissions to the radiative forcing budget, and the most precise spectroscopic parameters possible are hence required. In this study, a novel high finesse THz cavity, providing an interaction length in excess of 1 km, has enabled highly resolved spectra, and quantification of the weak transitions of CF$_4$ by cavity ring-down spectroscopy (CRDS). More than 50 pure rotational $P_6 - P_6 : \nu_3 - \nu_3$ lines of CF$_4$ have been measured, yielding both position and intensity with unequalled precision. Several tetrahedral splittings are fully resolved and measured with sub-MHz accuracy. Moreover, CRDS-THz allows determining absolute intensities and, using a global fit of the ν_2 polyad series, a CF$_4$ dipole parameter, namely $\tilde{\mu}_{3,3}$, has been fitted to 106.38(53) mD. This value is in very good agreement with that of the *ab initio*-based parameter deduced from a dipole moment surface. For the first time, a set of *ab initio* effective dipole moment parameters is derived for the computation of the transitions of the type $P_n - P_n$ ($n = 0, \ldots, 8$) and the resulting line list composed of 25 863 transitions can be used to model the whole CF$_4$ rotational spectrum. Finally, the TFMeCaSDa database is updated and is available for future spectroscopic and monitoring activities.

^{a} *Laboratoire de Physico-Chimie de l'Atmosphère, UR 4493, LPCA, Université du Littoral Côte d'Opale, F-59140 Dunkerque, France.*
  E-mail: arnaud.cuisset@univ-littoral.fr
^{b} *Groupe de Spectrométrie Moléculaire et Atmosphérique, UMR CNRS 7331, BP 1039, F-51687, Reims Cedex 2, France*
^{c} *Laboratoire Interdisciplinaire Carnot de Bourgogne, UMR 6303 CNRS - Université de Bourgogne, 9 Av. A. Savary, BP 47870, F-21078 Dijon Cedex, France*
† Electronic supplementary information (ESI) available: (1) Full list of fitted effective Hamiltonian parameters. (2) Room-temperature CF$_4$ line list in the range of 4–82 cm^{-1} calculated from an *ab initio* effective model. See DOI: **https://doi.org/10.1039/d4cp00653d**

1 Introduction

It is generally accepted in the public consciousness that greenhouse gases are synonymous with carbon dioxide CO$_2$. The media warn of the need to reduce CO$_2$ emissions. All over the world, carbon capture use and storage (CCUS) technologies are being developed to achieve zero-carbon emissions, CO$_2$ being the principal target. However, the contribution of other greenhouse gases to global warming, which may be less abundant than CO$_2$, is far from negligible. This is typically the case for tetrafluoromethane CF$_4$: with an atmospheric concentration almost five million times weaker than that of CO$_2$, this molecule has a warming power 6500 times greater and a lifetime 200 times longer (50 000 years) in the atmosphere.[1] Although less abundant, CF$_4$'s residual radiative forcing is much greater, and our atmosphere takes much longer to get rid of it. As a result, we can expect CF$_4$'s contribution to global warming from greenhouse gases to increase over the next few years. A study published in 2016 warned of a slowdown in the decline in perfluorocarbon (PFC) emissions and urged PFC generating industries especially aluminium and semiconductor manufacturing industries to continue to reduce the emissions of these potent greenhouse gases, which, once emitted, will stay in the atmosphere essentially permanently (on human timescales) and contribute to radiative forcing.[2] More recently, long-lived atmospheric greenhouse gases have been compared using IASI/Metop and ACE-FTS satellite and AGAGE ground-based measurements over the last 15 years.[3] These three instruments were found to demonstrate a remarkable degree of agreement in monitoring the atmospheric CF$_4$, and the concentration has been increasing linearly at a rate of 0.8 ppt per year ($\simeq$1% of

This journal is © the Owner Societies 2024

Phys. Chem. Chem. Phys., 2024, **26**, 12345–12357 | **12345**

the average atmospheric concentration) since 2008. These analyses were based on the inversion of the absorption spectrum of the strong ν_3 stretching fundamental band of CF_4 observed in the 1283 cm^{-1} region.[1]

Therefore, the accuracy of CF_4 monitoring depends on the accuracy of modelling of the ν_3 rovibrational band including line frequencies, intensities, air-broadening coefficients and profiles up to high J levels. In addition to the fundamental band, the main hot bands involving the lower rovibrational levels such as $\nu_3 + \nu_i - \nu_i$ with i = 1, 2 and 4 must be included since they contribute 92% of the total absorption at room temperature. This was the objective of a study in which a global analysis of 17 rovibrational bands of CF_4 was undertaken.[4] The first Terahertz (THz) measurements of the very weak rotational transitions of CF_4 in the $\nu_3 = 1$ state ($\nu_3 - \nu_3$ hot band) were included. Synchrotron-based Fourier transform spectroscopy was used with an optical path of 150 m with a white-type multipass cell, allowing recording of $R(20)$ to $R(37)$ line clusters in the 20–37 cm^{-1} (600–921 GHz) region at a resolution of 0.1 cm^{-1}. Due to a lack of sensitivity and resolution, the recorded THz lines were pressure-broadened ($P \simeq 100$ mbar) and largely averaged (5000 co-additions).[5] As a result, these measurements are characterised by high levels of uncertainty both in frequency and in intensity. Moreover, the tetrahedral splitting of CF_4 rotational lines was only very partially resolved. More recently, it has been demonstrated[6] that THz Fabry–Perot absorption spectroscopy with a km effective path length allowed detection of CF_4 THz lines with intensities lower than 1×10^{-27} cm^{-1} / (molecule cm^{-2}) and full resolution of the tetrahedral splitting. In this study, only the $R(20)$ cluster was measured with the unique consideration of line frequencies.

Here, a similar experimental setup described previously[7] is used, a cavity ring-down spectroscopy (CRDS) configuration has enabled the direct measurement of the absorption coefficient.[8] $R(19)$ to $R(30)$ and $Q(32)$ to $Q(34)$ line clusters are measured both in frequency and intensity with unequalled precision. CRDS THz line frequencies and intensities are included in a global fit of the ν_2 polyad (see Section 5.1) allowing an improvement of the RMS deviation and an accurate determination of the $\mu_{3,3}$ dipole moment parameter specific to the $\nu_3 - \nu_3$ CF_4 transitions. Fluoride-containing molecules are heavy species with highly congested spectra composed of many hot bands, even at room temperature. Recently, the complete elucidation of the dense and complex band structure in the rotationally resolved spectra of the greenhouse CF_4 and SF_6 molecules was made possible using accurate *ab initio* and variational calculations.[9,10] In this work, a non-empirical, *ab initio*-based effective model has been derived for the first time for the modelling of the whole CF_4 rotational spectrum. The quality of the resulting calculated line list has been validated by a direct comparison with experiment. Finally, this work has enabled an updated line list of CF_4 to be tabulated in the TFMeCaSDa database while the *ab initio* predictions pave the way for future experimental studies and line-by-line analyses.

2 THz cavity ring-down spectrometer

Observation of the weak CF_4 transitions around 20 cm^{-1} is beyond the sensitivity limits of a standard spectrometer with a single path absorption cell.[11] To perform high-resolution measurements of weakly absorbing species in this region, we have developed a cavity assisted THz spectrometer.[7,8] The excellent resolution is provided by an electronic source, which is an amplified multiplier chain (AMC). A standard microwave synthesizer is used to feed the AMC with 0 dBm in the range from 7.92 to 8.75 GHz. Once the frequency of the synthesizer has been multiplied by the AMC ($\times$72) it directly addresses the range from 570 to 630 GHz, or 19 to 21 cm^{-1}. Typical power levels in the rectangular waveguide at the AMC output are -2 dBm. The excellent resolution that can be achieved by such sources is possible due to their spectral purity, the emission linewidth is estimated to be around 1 kHz. Up-converting a microwave synthesizer provides two useful advantages. First, it allows the source to be readily modulated in both frequency and amplitude, and second, a traceable reference frequency can be easily introduced, in our case, a timing signal generated by a GPS receiver (Spectracom EC20S) was employed.

In order to increase the available sensitivity and consequently the accuracy of line measurements, a high finesse cavity was used to extend the interaction length between the sample gas and the THz radiation. The cavity is composed of two photonic mirrors and a corrugated waveguide, both designed for operation around 20 cm^{-1}. The radiation from the AMC source is launched into free space with a horn antenna before being coupled to the cavity using a TPX lens, see Fig. 1. The output of the cavity is refocused using a second TPX lens onto a zero biased detector (ZBD). The cavity has a free spectral range of 310 MHz, and finesse values of 4000 are routinely obtained, providing an interaction length of 1.2 km for a measurement cell that has a physical length of around 50 cm. To measure the narrow molecular transitions, both the AMC frequency and cavity mode must be simultaneously scanned over the zone of interest. This is achieved by finely adjusting the cavity length by means of two piezoelectric actuators; further details can be found elsewhere.[7] This instrument can be used to make not only cavity enhanced absorption spectroscopy (CEAS) measurements but also CRDS, the latter is of particular interest and has been used for this study as it directly gives a quantitative value of the absorption coefficient.[8]
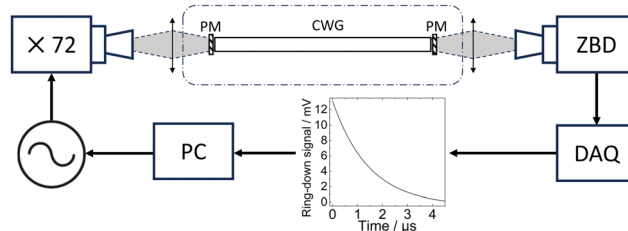

Fig. 1 THz cavity ring-down spectroscopy setup. An AMC source coupled to a resonant cavity itself composed of two photonic mirrors (PM) and a corrugated waveguide (CWG). The output of the cavity is measured by a ZBD whose signal is recorded using a data acquisition system (DAQ). The cavity is placed inside a low pressure gas chamber, as indicated by the dashed-dotted line.

The principle of CRDS is to measure the residency time τ of the photons in the cavity. The presence of an absorbing gas in the cavity will lead to a decrease in τ compared to the initial value under vacuum conditions. To measure the cavity ring-down time τ the AMC must be coupled to the cavity to allow the intracavity power to build up. Once a stable power level is obtained the source must be rapidly removed, achieved using pulse modulation, and the acquisition process is triggered. The light exiting the cavity is measured as a function of time and averaged for a large number of ring-down events, in our case 5×10^4 events per second. The signal from the detector is amplified and then measured using a dedicated data acquisition card (Spectrum Instruments) that samples at 1.25 GS s^{-1} and calculates the average waveform in real time. Each average waveform is fitted by an exponential function to give the value of τ.

3 Experimental results

Pure CF_4 ($>99.997\%$) purchased from Messer was introduced into the empty measurement chamber. A pressure of 0.2 mbar was selected to maximise the molecular signal while maintaining narrow linewidths, optimising the available molecular signal to noise ratio (SNR). The cavity is sensitive to temperature which results in slow changes to the baseline. A second spectrum is recorded, with an empty chamber, immediately after the acquisition of the molecular spectrum. The total duration is a compromise between the degree of data accumulation that is employed and the minimisation of the variation of the baseline. The measurement of a single line with its baseline is typically completed within 10 minutes. If no baseline spectrum is available a synthetic baseline can be produced using a suitable low order polynomial function. All CRDS spectra have been obtained at room temperature (294.0(15) K), with a frequency step size of 100 kHz. This step size was selected to match the mode width of the cavity, which provides around 20 measurement points within the FWHM of the lines. A typical example spectrum with its baseline is shown in Fig. 2. The difference in the cavity ring-down time with and without gas is clearly distinguished for three molecular lines of CF_4 separated by about 7 MHz (0.0002 cm^{-1}). The equivalent interaction length here is calculated to be 850 m with a cavity finesse of 2800. A total of 54 transitions, from 577.405 GHz to 629.164 GHz (19.26 cm^{-1} to 20.99 cm^{-1}), have been probed in this study. Nineteen of them are isolated so they have been individually resolved, while the remaining 35 could not be individually isolated due to the Doppler broadening at room temperature ($\simeq 0.8$ MHz (FWHM)). In this case, the measured absorption results from two or three overlapping molecular transitions. The use of CRDS has enabled the quantification of 28 (single or multiplet) line intensities.

The cavity ring-down time with and without gas, $\tau(\nu)$ and $\tau_0(\nu)$, respectively, are directly related to the molecular absorption coefficient $\alpha(\nu)$ (cm^{-1}):[12]

$$\alpha(\nu) = \frac{1}{c}\left(\frac{1}{\tau(\nu)} - \frac{1}{\tau_0(\nu)}\right) \qquad (1)$$

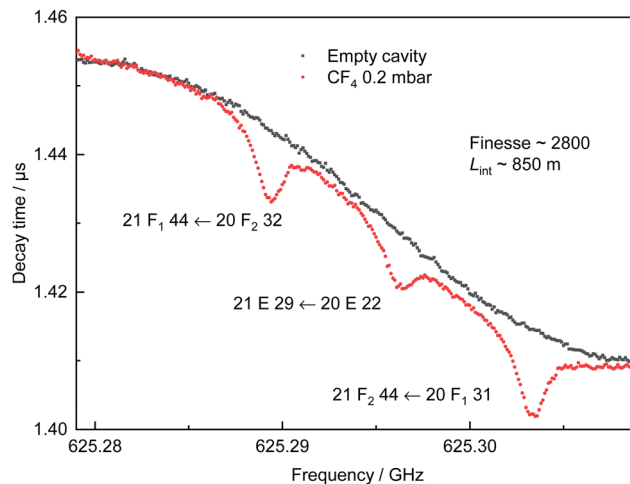where c is the speed of light (cm s^{-1}) and ν is the frequency (Hz)

Fig. 2 A CRDS spectrum and its baseline probing 3 rotational transitions of CF_4. Black points, cavity under vacuum conditions. Red points, CF_4 at 0.2 mbar. Each point is the average of 10^5 ring-down events. Step size 100 kHz, total acquisition time 600 s.

of the radiation. CRDS does not require a calibrated sample in order to perform quantitative absorption measurements. Knowledge of the physical length of the cavity is also not necessary. For the previous example $\alpha(\nu)$ is calculated directly from the CRDS spectrum and baseline and is shown in Fig. 3. Alternatively, the spectrum in Fig. 4 corresponds to 3 transitions of CF_4 with less than 100 kHz between the calculated line centres. The Doppler broadening of $FWMH_{Doppler} = 823$ kHz prevents the individual transitions from being resolved. This line displays a peak absorption of around 2.6×10^{-7} cm^{-1} resulting from a change of 30 ns in τ. Here, the mirrors are operating in the centre of the forbidden band optimising the cavity performance with $\tau = 2$ μs, a finesse of 3900, and an
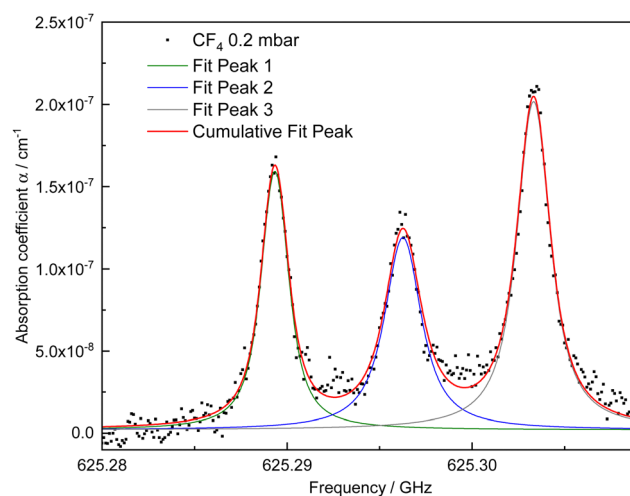

Fig. 3 The absorption coefficient spectrum determined from the CRDS spectrum in Fig. 2. Three Voigt functions sharing the same Gaussian line broadening contribution are used to obtain the cumulative fit of these transitions with overlapping tails (21 F_1 44 ← 20 F_2 32), (21 E 29 ← 20 E 22), and (21 F_2 44 ← 20 F_1 31).

This journal is © the Owner Societies 2024

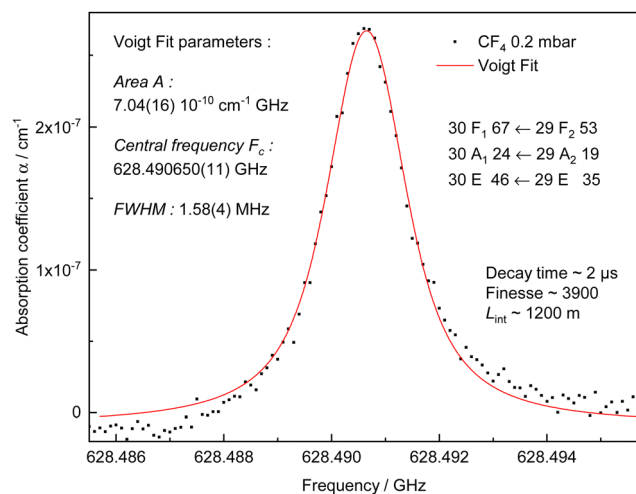*Phys. Chem. Chem. Phys.*, 2024, **26**, 12345–12357 | **12347**

Fig. 4 Absorption spectrum of 3 CF$_4$ transitions, the line centred frequencies are separated by less than 100 kHz so they cannot be resolved due to the Doppler broadening. Acquisition with a step size of 100 kHz, and 1×10^5 ring-down events are averaged to obtain a single frequency point, and a total acquisition time of 220 s is required to obtain a complete spectrum. A single Voigt function with a fixed Gaussian contribution is used to fit the absorption profile.

interaction path length of 1.2 km from a 48 cm length cavity. The smallest quantifiable variation in α is estimated to be 2×10^{-8} cm^{-1} for this configuration.

The spectra measured in this way are fitted with a Voigt profile, whose parameters are all free other than Doppler broadening which is fixed to its calculated value. No Voigt profile variations may be observed due to the limited SNR of the weak intensities of the CF$_4$ rotational transitions. The integrated absorption coefficient $A = \int \alpha \mathrm{d}\nu$ in cm^{-2}, line centre frequency ν_{exp} and linewidth in cm^{-1} are extracted from the fitting procedure. The transition line intensity I_{exp} is determined by dividing A by the molecular density n in molecule cm^{-3} determined by the gas equation $n = \dfrac{P}{k_{\mathrm{B}}T}$, while ν_{exp} is compared with the calculated value ν_{calc}, as presented in Table 1. The precision of ν_{exp} is estimated using the measured linewidth and SNR, as explained in the following section. For multiplet lines, we indicate in Table 1 the different assignments and calculated frequencies; we detail this case in Section 5.2. For example, in Fig. 4, the three transitions are fitted using a single Voigt function of fixed Gaussian contribution.

4 Uncertainties

The experimental uncertainty of ν_{exp} is evaluated by eqn (2) where FWHM is the linewidth and $\delta\nu$ is the frequency step size.[13]

$$\Delta\nu_{exp} = \frac{0.979\sqrt{\mathrm{FWHM}\,\delta\nu}}{\mathrm{SNR}} \tag{2}$$

The FWHM is obtained from the Voigt fitting procedure, and in our case $\delta\nu$ was held constant at 100 kHz. As regards the evaluation of the SNR, a prudent estimation was adopted. The

signal amplitude was simply the maximum value of the absorption coefficient. The noise amplitude was determined from the maximum peak-to-peak value present in the first and last 5 percent of the spectrum.

The line intensity uncertainty ΔI_{exp} was calculated by taking into account the precision of the pressure gauge, knowledge of the measurement cell temperature and the quality of the fitted absorption profile. The pressure gauge error is smaller than 0.001 mbar, and the temperature was controlled at 294.0(15) K. The quality of the fit is limited by the stability of the baseline which is not always perfectly removed, as can be observed in Fig. 4. The Voigt profile was minimised using OriginLab® software which provides a confidence interval ΔA equal to the estimated standard deviation of A. The different contributions were combined by eqn (3) and are included in Table 1.

$$\frac{\Delta I_{exp}}{I_{exp}} = \frac{\Delta A}{A} + \frac{\Delta T}{T} + \frac{\Delta P}{P} \tag{3}$$

The average relative uncertainties of the CRDS measurements are $\simeq 10^{-5}$% for the frequencies and $\simeq 10$% for the intensities. Compared to the synchrotron FT-IR measurements,[14] the frequency and intensity uncertainties are improved by factors 200 and 2, respectively. In a weighted global fit including IR data, such an accuracy improvement yields a significant influence of the THz rotational lines even with a modest number of lines. This was demonstrated for the THz measurements of the CH$_4$ centrifugal distortion induced rotational transitions,[15] in the case of CF$_4$ it will be verified in Section 5.1.

5 Analysis and discussion

The idea of introducing effective Hamiltonians $\tilde{H}(\tilde{t})$ for the modelling of absorption spectra of molecules whose energy levels are organized as small groups of nearly degenerate vibrational states, called polyads, has been well established for decades.[16,17] Currently, there exists two different ways for constructing effective Hamiltonians:

Case 1: effective parameters of a phenomenological model are obtained by a direct fit to experiment using a least-squares method (see Section 5.1). The same holds for the construction of an effective dipole moment operator (see Section 5.2). In this context, the approach proposed in ref. 18 is relevant for spherical top molecules.

Case 2: a non-empirical effective model is derived by applying a series of unitary transformations to the nuclear-motion Hamiltonian, composed of a kinetic energy operator and an *ab initio* potential energy surface (PES). Here, the numerical method proposed in ref. 19 is preferred to the commonly used Van Vleck transformations because the dipole moment parameters can be obtained from a dipole moment surface (DMS) without performing tedious algebraic calculations (see Section 5.3).

For both cases, each polyad is characterized by a polyad number

12348 | *Phys. Chem. Chem. Phys.*, 2024, **26**, 12345–12357

This journal is © the Owner Societies 2024

Table 1 Experimentally observed line frequencies ν_{exp} and intensities I_{exp} compared with the calculated values (ν_{calc}, I_{calc}) obtained from the fit (see Sections 5.1 and 5.2). $I_{ab\ initio}$ are the intensities obtained from the *ab initio* effective model (see Section 5.3). For unresolved line clusters, the experimental intensity I_{exp} is that of the cluster as a whole and the intensity of each component can be obtained through eqn (7). Line frequencies are given in GHz. Line intensities in units of cm^{-1} / (molecule cm^{-2}) which have been multiplied by 1×10^{27}. The experimental uncertainties are given in parentheses

Transition								$I_{exp} \times 10^{27}$	$I_{calc} \times 10^{27}$	$I_{ab\ initio} \times 10^{27}$
J''	C''	α'	J'	C'	α'	ν_{exp} / GHz	ν_{calc} / GHz	cm^{-1} / (molecule cm^{-2})		
19	A_2	11	20	A_1	15	595.825800(106)	595.825626	4.57(54)	3.75	4.22
19	A_2	12	20	A_1	16	596.518640(272)	596.518587	3.00(54)	2.71	3.05
19	A_1	10	20	A_2	14	595.848490(110)	595.848163	2.77(56)	3.69	4.14
19	F_2	30	20	F_1	41	595.832630(175)	595.832384	2.77(55)	2.24	2.51
19	F_2	31	20	F_1	42	596.205100(285)	596.205017	1.32(30)	1.91	2.15
19	F_1	31	20	F_2	42	595.840010(179)	595.839828	2.85(48)	2.23	2.50
19	F_1	32	20	F_2	43	596.114480(329)	596.114288	—	—	—
19	F_1	33	20	F_2	44	596.311630(380)	596.311646	—	—	—
20	A_2	11	21	A_1	14	625.730970(39)	625.731006	4.62(25)	3.50	3.93
20	A_1	12	21	A_2	16	625.584540(48)	625.584555	4.96(36)	3.77	4.29
20	A_1	13	21	A_2	17	626.471100(47)	626.471092	2.04(21)	2.21	2.49
20	E	22	21	E	29	625.296260(75)	625.296234	1.74(23)	1.65	1.86
20	E	24	21	E	31	626.464170(165)	626.464052	—	—	—
20	F_2	32	21	F_1	44	625.289340(57)	625.289361	2.54(25)	2.48	2.80
20	F_2	33	21	F_1	45	625.656590(91)	625.656716	2.01(22)	2.09	2.45
20	F_2	34	21	F_1	46	625.839690(78)	625.839690	2.10(28)	1.97	2.29
20	F_1	31	21	F_2	44	625.303320(50)	625.303327	3.38(23)	2.47	2.77
20	F_1	32	21	F_2	45	625.617060(80)	625.617183	1.93(19)	2.20	2.50
20	F_1	34	21	F_2	47	626.466270(116)	626.466375	—	—	—
27	A_1	16	28	A_2	21		587.307807		1.94	2.23
27	E	33	28	E	43	587.307750(110)	587.307609	4.21(43)	0.77	0.89
27	F_1	51	28	F_2	64		587.307807		1.16	1.32
27	F_2	48	28	F_1	63	589.437590(73)	589.437532	4.19(27)	1.58	1.82
27	F_1	50	28	F_2	65		589.437528		1.58	1.83
28	A_2	17	29	A_1	21		610.106098		2.77	3.20
28	E	34	29	E	44	610.106060(38)	610.106093	5.64(26)	1.11	1.27
28	F_2	51	29	F_1	67		610.106095		1.66	1.91
28	A_1	16	29	A_2	19		586.724152		1.64	1.77
28	E	30	29	E	35	586.724190(71)	586.724132	3.21(28)	0.66	0.70
28	F_1	44	29	F_2	53		586.724139		0.99	1.05
29	A_2	16	30	A_1	19		606.278291		2.35	2.53
29	E	30	30	E	37	606.278270(41)	606.278287	4.27(20)	0.94	1.00
29	F_2	45	30	F_1	53		606.278288		1.41	1.51
29	A_2	19	30	A_1	24		628.490594		2.18	2.52
29	E	35	30	E	46	628.490650(36)	628.490688	4.72(29)	0.87	1.00
29	F_2	53	30	F_1	67		628.490657		1.31	1.50
30	A_2	16	31	A_1	19		626.603820		1.84	1.98
30	E	32	31	E	37	626.603890(49)	626.603964	3.52(22)	0.74	0.79
30	F_2	48	31	F_1	58		626.603916		1.11	1.19
30	F_2	47	31	F_1	57	626.381980(35)	626.381977	3.63(24)	1.48	1.58
30	F_1	46	31	F_2	55		626.381973		1.48	1.58
31	A_1	16	31	A_2	24		577.405098		2.21	2.46
31	E	32	31	E	47	577.405100(148)	577.405104	3.74(54)	0.88	0.99
31	F_1	49	31	F_2	70		577.405102		1.33	1.48
32	A_1	18	32	A_2	24		592.046796		1.70	1.90
32	E	34	32	E	49	592.046540(64)	592.046330	3.11(20)	0.68	0.76
32	F_1	50	32	F_2	73		592.046486		1.02	1.14
32	F_2	50	32	F_1	72	594.991100(118)	594.991007	3.73(52)	1.36	1.52
32	F_1	49	32	F_2	74		594.991008		1.36	1.52
33	A_2	18	33	A_1	24		612.305429		2.31	2.55
33	E	34	33	E	50	612.305440(49)	612.305457	4.69(22)	0.93	1.03
33	F_2	51	33	F_1	76		612.305448		1.39	1.54
34	F_2	53	34	F_1	77	629.163980(66)	629.163941	2.76(20)	1.39	1.55
34	F_1	52	34	F_2	78		629.164005		1.39	1.55

$$P = c_1\nu_1 + c_2\nu_2 + \cdots + c_{N_m}\nu_{N_m} \qquad (c_i \in \mathbb{R}_{>0}), \qquad (4)$$

and the associated set of Hamiltonian parameters $\{\tilde{t}\}_P$ is obtained either by direct fitting to experimental data (Case 1) or from *ab initio* PESs (Case 2). In eqn (4), ν_i is the vibrational quantum numbers and N_m is the number of vibrational modes. By definition, the first polyad is $P = 0$, or simply denoted as P_0.

Although the second polyad does not necessarily equal $P = 1$, it is denoted as P_1, and so on. Success in the line-by-line analysis of high-resolution spectra thus lies in a convenient choice of the polyad vector $c = (c_1, c_2, \cdots, c_{Nm})^t$ in order to include the most relevant resonance coupling terms. In the case of quite isolated polyads with few vibrational bands, the approach proposed in (case 1) allows obtaining very accurate results using few

parameters. Conversely, for more complex polyads containing many vibrational bands, a proper characterization of all the resonance couplings becomes a challenging task. In this case, missing information on the so-called "dark" states may lead to a poor determination of some resonance coupling parameters, making the approach defined in (case 2) more relevant.

Note that the accuracy of the *ab initio* effective parameters $\{\tilde{t}\}_P^{ab\ initio}$ derived in (case 2) is typically that of the PES. These parameters can be thus further optimized by fine tuning to experimental data as in (case 1). We can also mention that for heavy molecules like CF_4 the density of lines dramatically increases because of the tremendous number of hot bands, resulting in strongly congested spectra, even at room temperature.

5.1 Inclusion in the global fit of line positions

Here, we used the present high-precision line positions to include them in the so-called "ν_2" polyad scheme already used in ref. 4. This scheme corresponds to a polyad vector $c = (0, 2, 6, 3)^t$ in which the $\nu_3 = 1$ level falls into the P_6 polyad (along with $\nu_4 = 2$). We can note that in this scheme, the ν_1 mode is ignored and there is no P_1 polyad (see the discussion in Section 5.4).

The general theory of the tensorial effective Hamiltonian can be found in many papers. The reader can for instance refer to ref. 18 and references therein. Let us just recall that for each polyad P_k, the effective Hamiltonian can be written in the form

$$\widetilde{H}_{\{P_k\}} = \sum_{\text{all indexes}} t_{\{s\}\{s'\}}^{\Omega(K,n\Gamma)\Gamma_v\Gamma'_v} \beta \left[{}^{\varepsilon}V_{\{s\}\{s'\}}^{\Omega_v(\Gamma_v\Gamma'_v)\Gamma} \otimes R^{\Omega(K,n\Gamma)} \right]^{(A_1)}. \tag{5}$$

In this equation, $t_{\{s\}\{s'\}}^{\Omega(K,n\Gamma)\Gamma_v\Gamma'_v}$ are parameters to be determined, while ${}^{\varepsilon}V_{\{s\}\{s'\}}^{\Omega_v(\Gamma_v\Gamma'_v)\Gamma}$ and $R^{\Omega(K,n\Gamma)}$ are vibrational and rotational operators, respectively. For each term, Ω_v and Ω represent the degree in elementary vibrational operators (creation a^+ and annihilation a operators), and rotational operators (components J_x, J_y and J_z of the angular momentum), respectively. β is a factor that allows the scalar terms (terms with $\Gamma = A_1$, the totally symmetric irreducible representation of T_d) to match the "usual"' contributions like $B_0 J^2$, *etc.* The order of each individual term is defined as $\Omega + \Omega_v - 2$.

Using this theory, we simply added the 54 $\nu_3 - \nu_3$ (as part of $P_6 - P_6$ transitions) line positions of Table 1 in the same "ν_2" global fit as in ref. 4 (see, in particular, Table 5 of this reference), using the XTDS[20] software package. We also took this opportunity to "clean" the fit by removing many duplicate assignments. A few $\nu_3 - \nu_3$ line positions that were already present in the fit were replaced with values from the present work. Thus, the $P_6 - P_6$ assignments has raised from 268 to 316. In Table 2, we compare the new fit statistics with those of ref. 4 Fig. 5 displays the fit residuals for line positions for the different transitions included in this global fit. Fig. 6 details the $\nu_3 - \nu_3$ ($P_6 - P_6$) part.

Although the combination of the elimination of duplicate lines and the introduction of the present new high-precision THz lines renders the comparison with the previous work somewhat tricky, we can tell that (i) we start from a more reliable line assignment list and (ii) the $\nu_3 - \nu_3$ region fit is influenced by the new lines. The overall root mean squares (RMS) deviation in the THz region has slightly decreased from 33.64 to 31.43 MHz. The 4.976 weighted standard deviation for the new THz lines may seem high, but this is due to strong constraints between data with very diverse experimental precisions in this fit; anyway, their RMS deviation of *ca.* 99 kHz is satisfactory. Some RMS deviations for other transitions have slightly increased compared to ref. 4 but, again, this is due to the "cleaning" of the global fit that has changed the weight of many lines with the removal of duplicates. In any case, it was mandatory to re-do the global fit of line positions in order to obtain consistent eigenvectors for the line intensity analysis. We give the full list of effective Hamiltonian parameters resulting from the present fit as ESI.†

5.2 Fit of effective dipole moment parameter

As a spherical top, CF_4 has no permanent dipole moment. But, following the same theory as the one explained in ref. 5, we consider here the effective dipole moment operator for $\nu_3 - \nu_3$ transitions in the form

$$\tilde{\mu}^{\langle \mu_3 - \mu_3 \rangle} = \tilde{\mu}^{\langle \mu_3 - \mu_3 \rangle}_{\{GS-GS\}} + \tilde{\mu}^{\langle \mu_3 - \mu_3 \rangle}_{\{\nu_3 - \nu_3\}}$$

$$= \tilde{\mu}_0 R^{2(2,F_2)} + \tilde{\mu}_{3,3}{}^+ V_{\{3\}\{3\}}^{2(F_2 F_2)F_2} + \cdots \tag{6}$$

Table 2 Fit statistics for line positions in the "ν_2" polyad scheme, compared to results of ref. 4 σ is the dimensionless standard deviation and d_{RMS} the root mean square deviation in 1×10^{-3} cm^{-1}, except for THz $\nu_3 - \nu_3$ lines for which it is given in MHz

	Ref. 4				This work			
Transitions	Nb. data	J_{max}	σ	$d_{RMS}/1 \times 10^{-3}$ cm^{-1}	Nb. data	J_{max}	σ	$d_{RMS}/1 \times 10^{-3}$ cm^{-1}
$P_2 - P_0$:ν_2	4686	82	0.9984	1.027	3744	82	1.009	1.043
$P_3 - P_0$:ν_4	2254	72	1.276	1.276	2198	72	1.115	1.115
$P_4 - P_0$:$2\nu_2$	823	42	0.7757	0.7757	602	42	0.989	0.989
$P_5 - P_0$:$\nu_2 + \nu_4$	877	39	1.188	1.188	862	39	1.188	1.188
$P_6 - P_0$:$\nu_3/2\nu_4$	2930	53	0.9847	1.161	2686	53	1.153	1.332
$P_8 - P_0$:$\nu_2 + (\nu_3/2\nu_4)$	4763	49	1.167	1.167	3554	49	1.176	1.177
$P_4 - P_2$:$2\nu_2 - \nu_2$	803	68	0.7758	0.7758	803	68	0.7588	0.7588
$P_6 - P_4$:$\nu_3 - 2\nu_2$	222	37	1.189	1.189	222	37	1.063	1.063
$P_6 - P_6$:$\nu_3 - \nu_3$	268	37	0.9173	33.64 MHz	316	37	2.858	31.43 MHz
Total	17 626	82	1.076	1.116	14 987	82	1.159	1.126

12350 | *Phys. Chem. Chem. Phys.*, 2024, **26**, 12345–12357
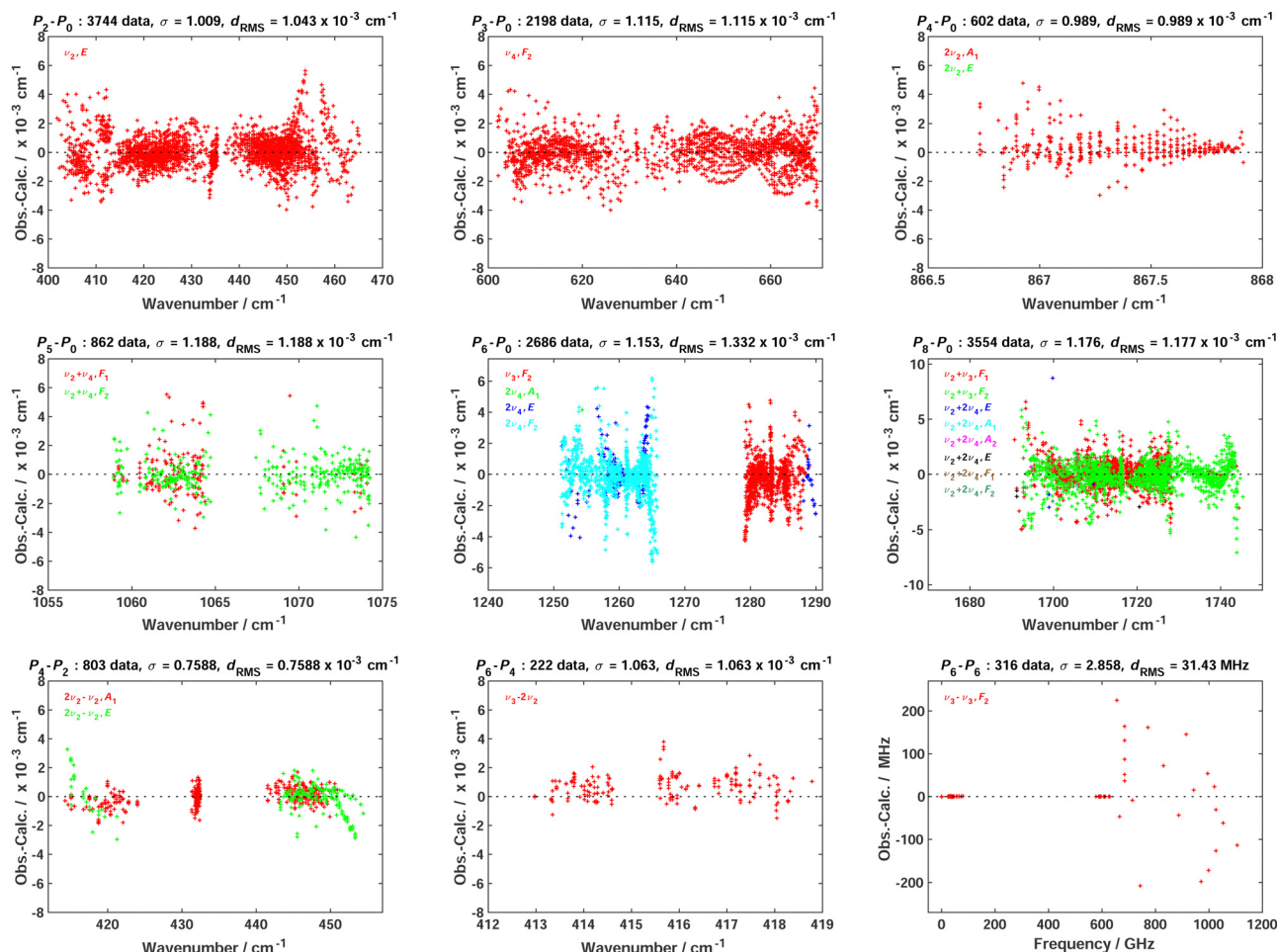
This journal is © the Owner Societies 2024

Fig. 5 Fit residuals for line positions in the global fit; each panel corresponds to a set of transitions between two polyads (see the text for polyad definition); σ is the dimensionless standard deviation and d_{RMS} is the root mean square deviation. This is to be compared with the equivalent Fig. 3 in ref. 4

This contains two terms in the right member. The first one, $\mu_{\{GS-GS\}}^{\langle\mu_3-\mu_3\rangle}$ corresponds to a centrifugal distortion-induced dipole moment in the ground state (GS) and should be very small. The second term is the dipole moment derivative that is specific to $\nu_3 - \nu_3$ transitions. The corresponding parameter $\mu_{3,3}$ can be fitted using the present intensity data.

The main problem when fitting effective dipole moment parameters using experimental data is that one needs to find and assign isolated lines in order to determine intensities of single transitions. However, as previously mentioned, for quite heavy molecules, there are generally line clusters consisting of superimposed transitions that cannot be resolved experimentally. This is the case for CF_4. Let us take an example from Table 1, the line at 587.307750 cm^{-1} is a triplet consisting of an $A_1 \rightarrow A_2$, an $E \rightarrow E$ and an $F_1 \rightarrow F_2$ transition. But the measured intensity, 4.21×10^{27} cm^{-1} / (molecule cm^{-2}), is the sum for these three transitions. Among the 30 measured intensities, 13 are such multiplets: 4 doublets and 9 triplets, the remaining 17 measurements corresponding to singlets. We have thus a potential of 52 transitions (which is much better than just using the 17 isolated lines), if we can extract individual line intensities for the multiplets. This is possible, since we know

their assignments, that is the transitions that compose them. The idea is to split experimental intensities between the multiplet components using the following procedure.

Due to the 1/2 spin of the F ligands, CF_4 have spin statistical weights w_i for each T_d symmetry species A_1, A_2, E, F_1 or F_2. It is easy to show[23] that these weights are 3, 3, 2, 5 and 5, respectively. Thus, for a cluster of $n = 2$ or 3 lines with experimental total intensity I_{exp}, the intensity of the "subline" i can be extracted as follows:

$$I_{exp}^i = \frac{w_i I_{exp}}{\sum_{j=1}^{n} w_j}. \tag{7}$$

We thus obtained 52 individual line intensities that we introduced in a fit, again using XTDS.[20] The 2 transitions 20 F_2 43 ← 19 F_1 32 (the line is too distorted to be fitted) and 20 F_2 44 ← 19 F_1 33 ($I_{exp} = 1.15 \times 10^{-27}$ cm^{-1} / (molecule cm^{-2}), uncertainty 34%) shown in Table 1 have not been taken in consideration for the line strength global fit, for experimental reasons (very low finesse attributed to a misalignment of the mirrors; one mirror may have hit against the waveguide during the experiment). It also appeared that two line intensities were
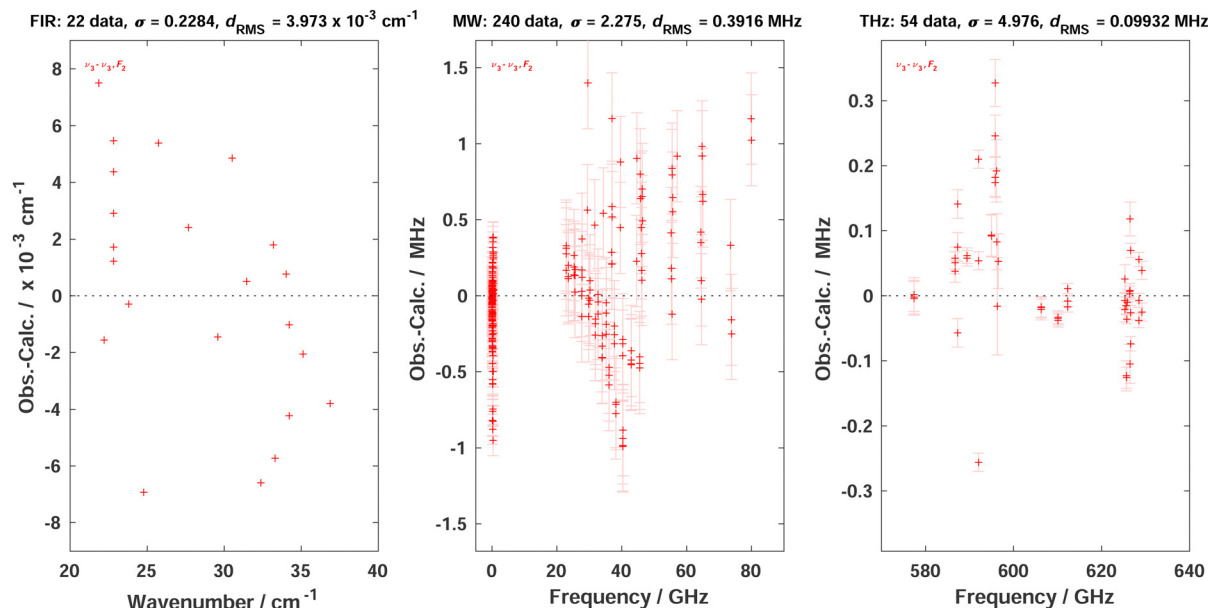
Fig. 6 Fit residuals for line positions in the global fit in the case of $P_6 - P_6$; σ is the dimensionless standard deviation and d_{RMS} is the root mean square deviation. The three panels detail these residuals for far-infrared (FIR) lines from ref. 5 infrared-microwave/radiofrequency (MW) lines from ref. 21, 22 and THz line from the present work. The last two panels also display experimental line position error bars. It should be noted that ref. 4 did not mention the MW lines from Takami *et al.* but those were already included in the global fit of this paper.

outliers that were removed from that fit. These 2 transitions, 21 E 31 ← 20 E 24 and 21 F_2 47 ← 20 F_1 34, separated by only 2.1 MHz, they are too close from each other to be reliably fitted for quantification.‡ These four transitions have been included in the global fit of line positions but, consequently, we finally end up with a fit of 50 experimental intensities. The resulting relative RMS deviation is 16.6% and the standard deviation is 1.706. We obtain the following parameters:

$$\tilde{\mu}_{3,3} = 106.38(53) \text{ mD} \qquad (8)$$

This value is somewhat higher than the 80 mD from ref. 5, but this one was a very rough estimate that did not result from a fit. All attempts to fit higher-order effective dipole moment terms were unsuccessful. The *ab initio* calculations presented in Section 5.3 confirmed that the next term in $\left(R^{1(1,\,F_1)} \otimes V_{3,3}{}^{F_2 F_2 (F_1)}\right)^{(F_2)}$ gives a contribution 4 orders of magnitude smaller than the pure vibrational term (8). To our knowledge, this is the very first time that a dipole moment parameter on CF_4 is fitted using directly intensity measurements for individual lines. Fig. 7 displays the fit residuals for line intensities. We see no systematic deviation as a function of the rotational quantum number J, confirming that there is no further fittable term using the present data. Fig. 8 compares the experimental intensities with the calculated ones, using either the above parameter or the *ab initio* lines (see Section 5.3 below). We also checked that the calculated far-infrared
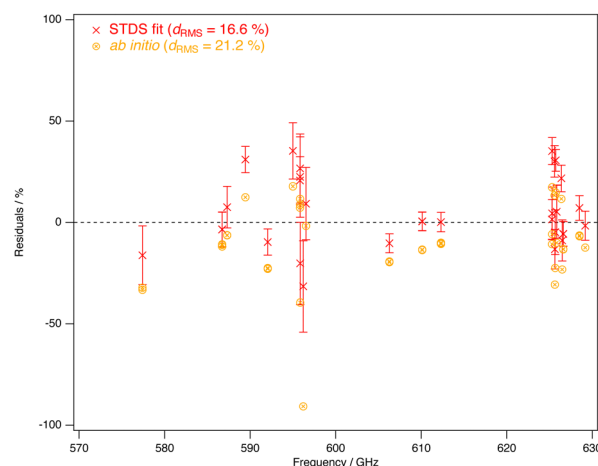
‡ NB: A multi Voigt fit with fixed frequency centers gives respectively $I_{exp} = 8.71 \times 10^{-28} \text{ cm}^{-1}$ / (molecule cm^{-2}) uncertainty 17% and $I_{exp} = 1.11 \times 10^{-27} \text{ cm}^{-1}$ / (molecule cm^{-2}) uncertainty 15%. If the frequency centers are let free, the fit diverges.

Fig. 7 Relative fit residuals for fitted and *ab initio* line intensities for the presently measured $\nu_3 - \nu_3$ THz lines, as a function of the frequency.

spectrum using the fitted effective dipole moment parameters compares well to the experimental spectrum from ref. 5, as shown in Fig. 9, to be compared with Fig. 1 of this previous paper. We used here a better simulation program[24] that better takes into account the instrumental parameters from the Fourier-transform spectrometer. This explains that the previous simulation, obtained thanks to a rougher simulation underestimated the parameter value. The spectrum calculated from the *ab initio* effective model described in Section 5.3 is also depicted in Fig. 9.

5.3 Derivation of *ab initio* effective dipole moment parameters

In ref. 9, more than 700 vibrational bands and subbands were predicted for CF_4 to construct a variationally computed line list

12352 | *Phys. Chem. Chem. Phys.*, 2024, **26**, 12345–12357

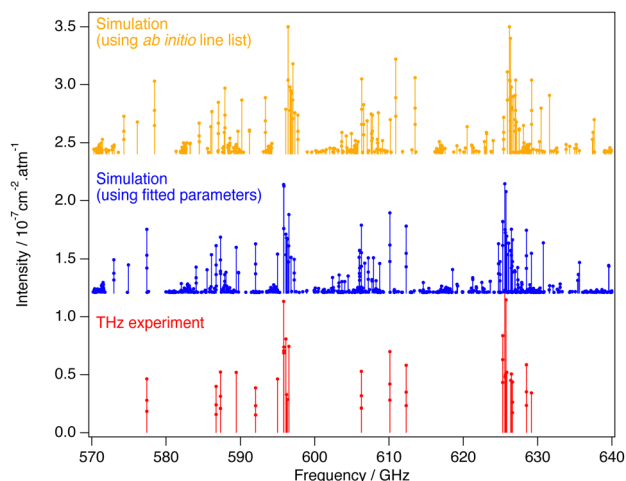This journal is © the Owner Societies 2024

Fig. 8 Comparison between THz experimental, fitted (using effective Hamiltonian and dipole moment) and *ab initio* lines computed in Section 5.3. Simulated line intensities have been shifted upward for clarity.

up 4000 cm^{-1}, composed of 2 billion rovibrational transitions at 296 K. Such a density of lines is obtained in methane spectra at 1000 K.[26] This list is freely available on the TheoReTS[27] webpages **https://theorets.univ-reims.fr**, **https://theorets.tsu.ru**. The accuracy of our *ab initio* line intensities was recently validated in different spectral ranges by a direct comparison with experiment.[28] Due to its relatively low-lying vibrational modes compared to other spherical top molecules like methane, the CF$_4$ rotational spectrum is composed of successive hot band transitions of the type $P_n - P_n$ ($n = 1, 2,\ldots$). We have fitted the parameter μ_{33} (8) of $P_6 - P_6$ using the "ν_2" polyad scheme.

For the modelling of the very crowded CF$_4$ spectra, we can consider an approach which is complementary to the one presented in Sections 5.1 and 5.2 and that combines both the small dimensionality of the spectroscopic models and the completeness of the variational calculation. Within that context, a novel methodology has been recently proposed in ref. 19 to construct an *ab initio* effective rotation–vibration spectroscopic model directly from a PES and a DMS. Very briefly, let $\mathbf{H}^{(J,C)}$ be the matrix representation of the complete nuclear-motion Hamiltonian for a given symmetry block (J,C), computed in a basis set $\{|\gamma;J,C\rangle\}$ where γ denotes all other symmetry labels and quantum numbers (v_i, *etc.*). For the CF$_4$ molecule, the *ab initio* PES and DMS of ref. 9 were employed and the Eckart–Watson Hamiltonian[29] was used to build $\mathbf{H}^{(J,C)}$ using harmonic oscillator basis functions. Then, we search for a unitary transformation $\mathcal{T}_P^{(J,C)}$ that brings $\mathbf{H}^{(J,C)}$ into block diagonal form up to a maximum polyad P_{N_P}

$$\mathbf{H}_{\text{Polyad}}^{(J,C,P)} = \left[\mathcal{T}_P^{(J,C)}\right]^{-1} \mathbf{H}^{(J,C)} \mathcal{T}_P^{(J,C)}$$
$$= \left[\mathbf{H}_{P_0}^{(J,C)} \oplus \cdots \oplus \mathbf{H}_{P_{N_P}}^{(J,C)}\right] \oplus \mathbf{H}_R^{(J,C)}, \quad (9)$$

by defining a consistent polyad scheme. In eqn (9), the last block $\mathbf{H}_R$ includes all the "remaining" polyads beyond P_{N_P}.

Unlike contact transformations[30] based on perturbation theory,[31] the approach proposed in ref. 19 obviates the need to make tedious algebraic calculations for the derivation of both Hamiltonian and dipole moment effective parameters. A brief inspection of the harmonic frequencies for CF$_4$ suggests to define the polyad vector as $\mathbf{c} = (0.8, 0.4, 1.2, 0.6)^t$. Using this scheme, the first polyads are: P_0 = ground state, $P_1 = \nu_2$, $P_2 = \nu_4$, $P_3 = \{\nu_1, 2\nu_2\}$, $P_4 = \nu_2 + \nu_4$, $P_5 = \{\nu_1 + \nu_2, 3\nu_2, \nu_3, 2\nu_4\}$, *etc.* In this paper, the matrix $\mathbf{H}_{\text{Polyad}}^{(J,C,P)}$ was constructed up to $P_{N_P} = P_8$ from a numerical procedure that took 5 hours using 28 processors, including the variational calculation up to $J = 10$ to compute $\mathcal{T}_P^{(J,C)}$. The choice of this polyad scheme compared to the one proposed in Section 5.1 will be discussed in Section 5.4.

At this stage, it is worth mentioning that $\mathbf{H}_{\text{Polyad}}^{(J,C,P)}$ in eqn (9) is nothing but a matrix representation of an effective Hamiltonian in a basis $\{|\gamma;J,C,P\rangle\}$, with a set of parameters $\{\tilde{t}\}_P^{ab\ initio}$ to be determined. The strategy thus consists in considering an effective Hamiltonian $\tilde{H}(\tilde{t})$ of the type (5) whose effective parameters are determined for each polyad P such that the matrix elements of $\tilde{H}(\tilde{t})$ match the elements of $\mathbf{H}_{\text{Polyad}}^{(J,C,P)}$. To this end, we follow the iterative procedure (19) of ref. 19. For line intensity calculation, we can define the transformed matrix

$$\tilde{\mathbf{M}}_\Theta = \left[\mathcal{T}_{P'}^{(J',C')}\right]^{-1} \mathbf{M}_\Theta \mathcal{T}_P^{(J,C)}, \quad (10)$$

where $\mathbf{M}_\Theta$ ($\Theta = X, Y, Z$) is the matrix of the laboratory-fixed frame dipole moment components $\left(C^{(\Gamma')} \otimes M^{(\Gamma)}\right)^{(\bar{\Gamma})}$ computed in the same primitive basis as the Hamiltonian. Here, $M_\alpha^{(\Gamma)} \equiv M_\alpha^{(\Gamma)}(\mu)$ ($\alpha = x, y, z$) are the molecular-fixed frame dipole moment components and the μ's are the *ab initio* DMS parameters of ref. 9. $C^{(\Gamma')}$ is the tensor counterpart[32] of the direction cosines $\lambda_{\Theta\alpha}$. Similarly, we determine the parameters $\tilde{\mu}$ of an effective normal-mode dipole moment operator $\tilde{M}_\alpha^{(\Gamma)}(\tilde{\mu})$ (see eqn (6)) such that the matrix elements of $\left(C^{(\Gamma')} \otimes \tilde{M}^{(\Gamma)}\right)^{(\bar{\Gamma})}$ match $\tilde{\mathbf{M}}_\Theta$. Only transitions with $J \leq 2$ are required to determine the effective dipole moment parameters.

In this work, we have developed the effective Hamiltonian (5) at order 8 up to the eighth polyad, except that the resulting 964 parameters have been determined directly from the PES, without any fit to experimental data. The effective dipole moment of the type (6) has been expended at order 6 and 723 vibrational parameters were simultaneously determined from the DMS for all the transitions $P_n - P_n$, $n = 0,\ldots, 8$. We have shown in this work that the contribution of the rovibrational terms to the line intensities of $P_n - P_n$ was negligible, by at least 4 orders of magnitude. Only one rotational parameter was included in the model for computing the $P_0 - P_0$ transitions and one rovibrational parameter was determined for $\nu_2 - \nu_2$, for which purely vibrational terms are not allowed by symmetry. Some terms of the tensor dipole moment are given below, with
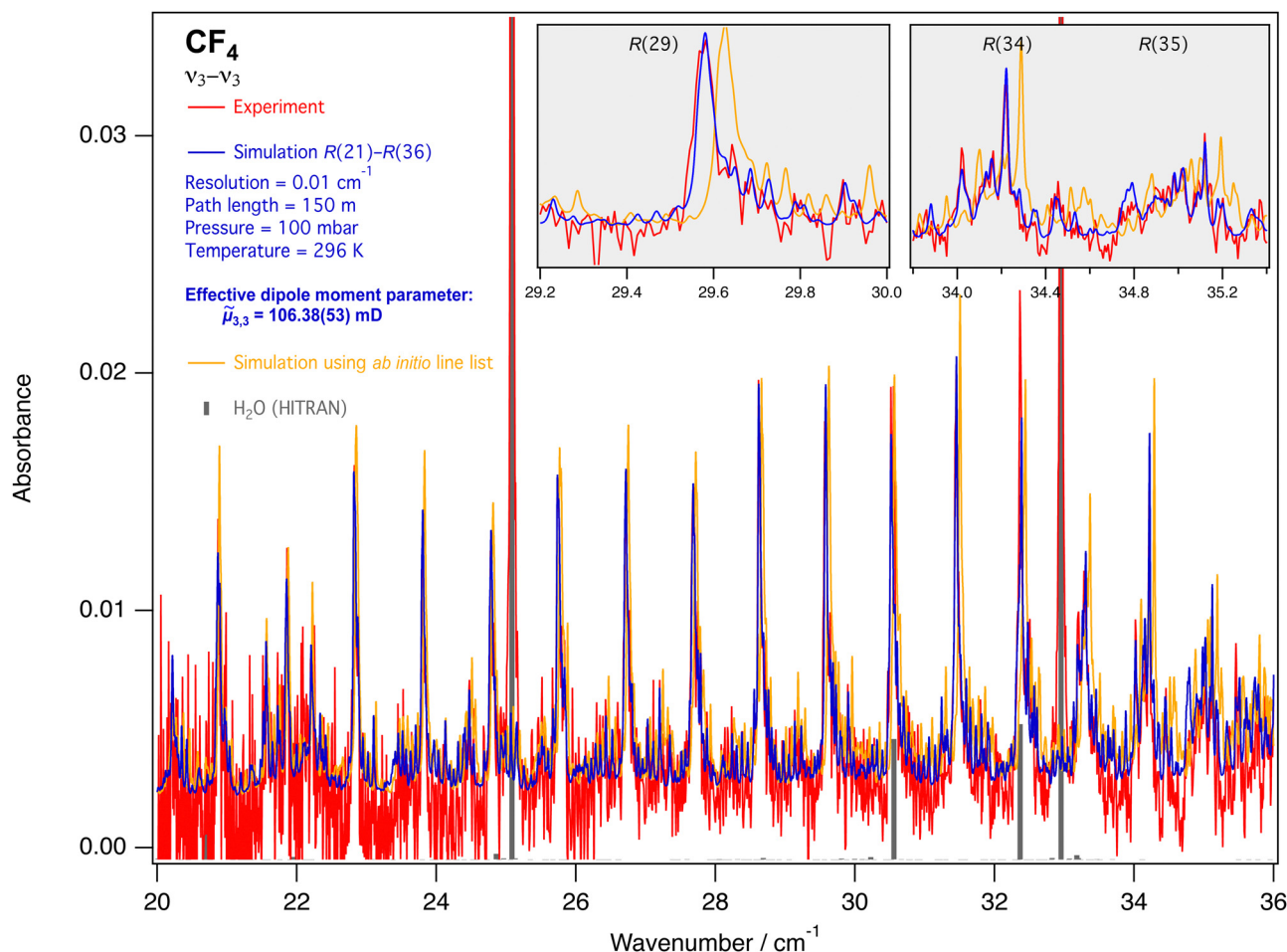
Fig. 9 FTIR spectrum of $\nu_3 - \nu_3$ lines in the R branch (from ref. 5), compared to the simulation. Grey ticks show water lines taken from the HITRAN database.[25] The insets detail three line clusters. The *ab initio* line list – with errors on the line positions estimated between 0.01 and 0.05 cm^{-1} – can be found in the ESI.†

parameters in units of 10^{-4} Debye:

$$
\begin{aligned}
\nu_3 - \nu_3 (P_5 - P_5) &\rightarrow 680.07\, V_{\{3,3\}}^{F_2 F_2(F_2)} + \cdots \\
\nu_3 - 2\nu_4 (P_5 - P_5) &\rightarrow 5.80\, V_{\{3,44\}}^{F_2 A_1(F_2)} \\
&\quad -3.23\, V_{\{3,44\}}^{F_2 E(F_2)} + \cdots \\
2\nu_4 - 2\nu_4 (P_5 - P_5) &\rightarrow 7.22\, V_{\{44,44\}}^{F_2 F_2(F_2)} \\
&\quad +8.45\, V_{\{44,44\}}^{F_2 A_1(F_2)} + \cdots \\
3\nu_2 - \nu_3 (P_5 - P_5) &\rightarrow 0.49\, V_{\{222,3\}}^{A_1 F_2(F_2)} \\
&\quad -0.17\, V_{\{222,3\}}^{E F_2(F_2)} + \cdots \\
4\nu_2 - \nu_2 + \nu_3 (P_7 - P_7) &\rightarrow -0.24\, V_{\{2222,23\}}^{F_1 F_2(F_2)} \\
&\quad +0.36\, V_{\{2222,23\}}^{E F_2(F_2)} + \cdots \\
\nu_2 + \nu_3 - \nu_2 + \nu_3 (P_7 - P_7) &\rightarrow 961.11\, V_{\{23,23\}}^{F_2 F_2(F_2)} + \cdots \\
\nu_3 + \nu_4 - \nu_3 + \nu_4 (P_8 - P_8) &\rightarrow 10.72\, V_{\{34,34\}}^{F_2 F_2(F_2)} + \cdots
\end{aligned}
\tag{11}
$$

Note that the definition of the irreducible tensor vibrational operators[33] used in eqn (11) differs from those in eqn (6) whereas the rotational part in the effective Hamiltonian and dipole moment operator is unchanged. We can show that these two sets of vibrational operators can be related by following

Appendix of ref. 19. We have plotted in Fig. 10 (upper panel) the strongest line intensities between 5 and 80 cm^{-1} using the *ab initio* dipole moment parameters. The line positions were computed from the pure *ab initio* effective Hamiltonian parameters at an accuracy estimated between 0.01 and 0.05 cm^{-1}. The line list is provided in the ESI.† Finally, in the experimental spectral range considered in this work, only $\nu_3 - \nu_3$ transitions have been observed (see Fig. 10, bottom panel). The corresponding *ab initio* effective parameter can be easily converted to the STDS formalism as

$$
\tilde{\mu}_{3,3}^{ab\,initio} = 117.8 \text{ mD.} \tag{12}
$$

The error between this value and that obtained from the fit in eqn (8) is close to 10%, which is within the RMS error of 16.6%. Fig. 8 shows the good agreement between the observed lines and those computed from the fitted and *ab initio* models, though the *ab initio* line positions were not computed at the spectroscopic accuracy. With the actual limit of detection of the THz CRDS technique, line intensities below 1×10^{-27} cm^{-1} / (molecule cm^{-2}) are difficult to measure (see Table 1). Fig. 10 explains why only $\nu_3 - \nu_3$ transitions were observed in the
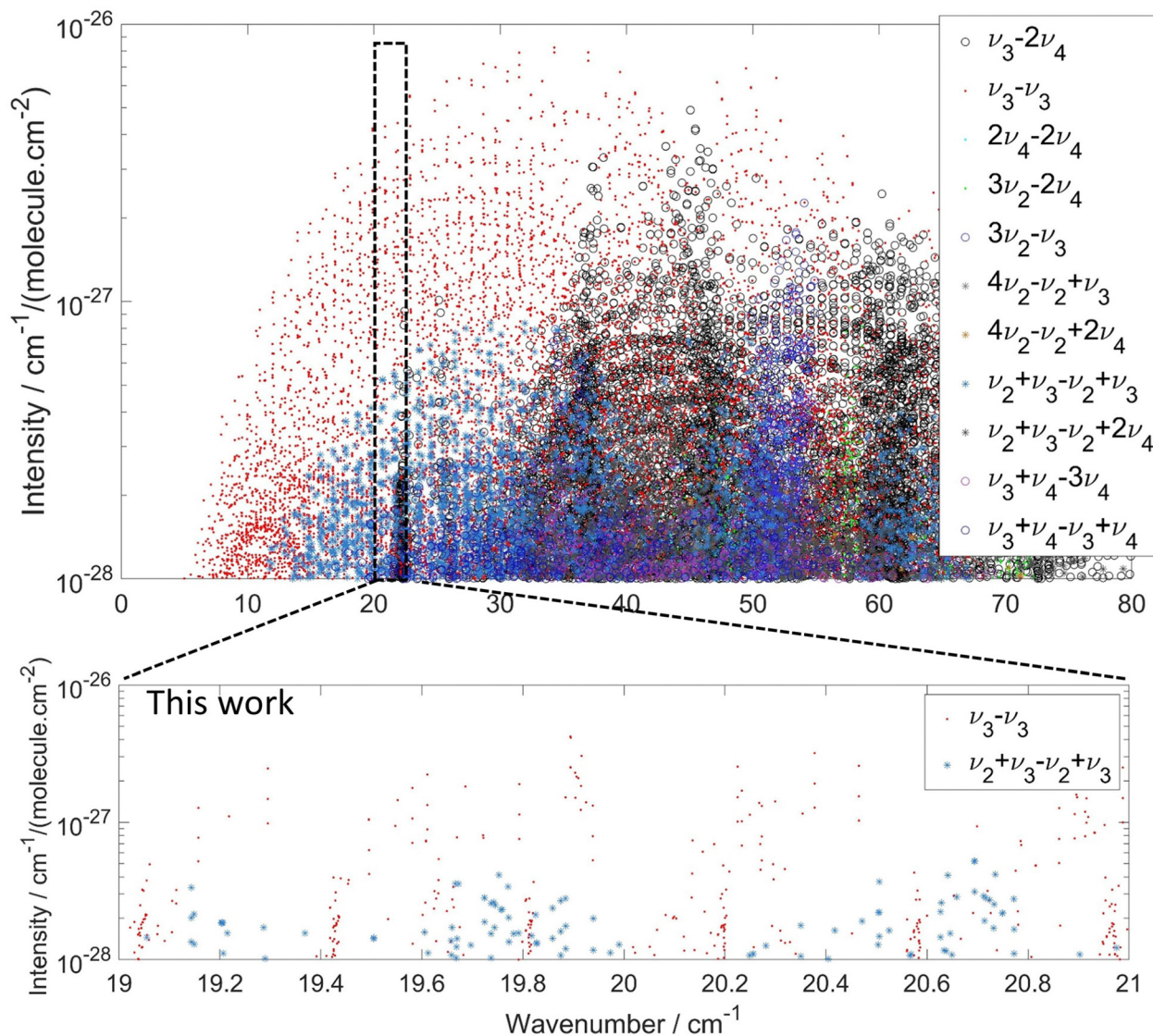
Fig. 10 (upper panel) Strongest line intensities of the rotational transitions for CF_4 using the *ab initio* effective "global" model described in Section 5.3. (bottom panel) Detailed portion of the *ab initio* line intensities in the observed range of the present work.

19–21 cm^{-1} region. This also explains why—contrary to CH_4[34,35]—the GS–GS and $\nu_4 - \nu_4$ transitions cannot be observed here because their associated parameters turn out to be 3 and 2 orders of magnitude smaller than those of methane, respectively. For example, our *ab initio* parameter μ_0 involved in (6) is estimated to ${\sim}0.056$ μD while the recommended value for methane is of ${\sim}22.5$ μD.

Line intensities of $\nu_3 - \nu_3$ in the observed spectral range and computed from the parameter $\tilde{\mu}_{3,3}^{ab\,initio}$ are given in the last column of Table 1. We can also compute the experimental and calculated (fit and *ab initio*) sum of intensities S $(\times 10^{26})$ in this range. We obtain $S_{exp} = 9.36$, $S_{fit} = 8.87$ and $S_{ab\,initio} = 9.91$ cm^{-1}/ (molecule cm^{-2}) and we can see that S_{exp} is between the two calculated values. Note that the two calculated sums differ by 10.5%, while a comparison between the fitted parameter $\tilde{\mu}_{3,3}$ (8) and the *ab initio* parameter $\tilde{\mu}_{3,3}^{ab\,initio}$ (12) would suggest a difference of 21%. A brief inspection of the eigenvector

decomposition showed that the treatment of the resonance coupling for the dyad system $\nu_3/2\nu_4$ slightly differs between the fitted and *ab initio* effective models. This thus explains why the difference between $S_{ab\,initio}$ is not that expected.

5.4 Effective *versus* "ab initio" polyad scheme: discussion

The choice of a relevant polyad scheme 4 is partly conditioned by the available observed data. In ref. 4 and in this work, the so-called "ν_2" polyad scheme was employed to build the empirically fitted effective Hamiltonian and dipole moment because of the lack of data for ν_1. The same holds for the bands $\nu_1 + \nu_2$ and $3\nu_2$ which were omitted in the polyad called P_5. For the construction of the *ab initio* model presented in Section 5.3, only PES and DMS are required. Most of the resonance couplings are taken into account in the *ab initio* model, even those associated with "dark" states that are not directly observable. Thus, the choice (4) based on some "resonance" conditions

This journal is © the Owner Societies 2024

Phys. Chem. Chem. Phys., 2024, **26**, 12345–12357 | **12355**

Table 3 Rovibrational transitions in TFMeCaSDa. The polyad sheme is described by the $(c_1, c_2, c_3, c_4)^t$ polyad vector as explained in Section 5

Transitions	Nb. dipolar	Dipolar wavenumber / cm^{-1}	Dipolar intensity / (cm^{-1} / (molecule cm^{-2}))
Scheme 1 $(0, 2, 6, 3)^t$			
$P_6 - P_0$	39 086	1230–1305	8×10^{-25}–8×10^{-22}
$P_3 - P_0$	15 149	583–682	8×10^{-27}–8×10^{-24}
$P_8 - P_2$	33 430	1231–1330	8×10^{-25}–1×10^{-20}
$P_6 - P_6$	284 350	1–114	1×10^{-30}–8×10^{-27}
Scheme 2 $(3, 0, 4, 2)^t$			
$P_6 - P_0$	3408	1270–1283	8×10^{-25}–1×10^{-21}
Total	375 423		

between the vibrational modes does not depend on available experimental data.

The "*ab initio*" polyad vector $(0.8, 0.4, 1.2, 0.6)^t$, also equals to $(4, 2, 6, 3)^t$, should allow inclusion of all possible resonance coupling terms inside a given polyad. In order to see the impact of removing ν_1 and its overtones, as in Section 5.1, an *ab initio* model was built using the scheme $(0,2,6,3)^t$ and the results have been compared to the "full" model. For a proper comparison, $\nu_1 + \nu_2$ and $3\nu_2$ were also removed from the model. Not surprisingly, many line positions of the "light" model were slightly shifted for the P_n–P_m ($n \neq m$) transitions with respect to the "full" model while both the line positions and line intensities of $P_n - P_n$ were similar in the range considered in this work. This can be explained by quite weak resonance couplings between $\nu_1 + \nu_2/3\nu_2$ and $\nu_3/2\nu_4$, making the "ν_2" polyad scheme relevant for the present study. For example, in the "full" model the rovibrational state $|J = 19, C = A_2, \alpha = 11\rangle$ involved in the first transition in Table 1 decomposes as $\sim$91.5% of $|\nu_3\rangle$, $\sim$8.5% of $|2\nu_4\rangle$ and less than 0.01% of $|\nu_1 + \nu_2\rangle$ and $|3\nu_2\rangle$.

6 CF$_4$ database update

The Dijon CF$_4$ database, also called TFMeCaSDa for tetrafluoromethane calculated spectroscopy database, and previously built using three different polyad schemes,[36] has been reviewed and updated. The third scheme, initially used to describe these pure rotational lines of $\nu_3 = 1$, and based on earlier work by Boudon *et al.*[14] has been removed. Instead, we have defined $P_6 - P_6$ in scheme 1, adding 284 350 new transitions in the 1 to 114 cm^{-1} range. This update is already available at **https://vamdc.icb.cnrs.fr/PHP/CF4.php** and will be the subject of a forthcoming publication detailing the latest major update to the Dijon CaSDa24 databases. Table 3 summarizes the changes in the database using this global approach. The total number of calculated lines has increased slightly, but their accuracy is better, as explained in Section 5.

7 Conclusions

Using THz CRDS, more than 50 pure rotational transitions $P_6 - P_6$:$\nu_3 - \nu_3$ of CF$_4$ have been measured both in frequency and intensity with unequalled precision. The experimental data have been included in a global fit of the ν_2 polyad series allowing "cleaning" of the previous line list and slight improvement of the overall RMS in the THz region. Moreover, it was possible for the first time to fit a CF$_4$ dipole moment parameter using absolute absorption coefficient measurements of individual tetrahedral splitting components, namely the $\tilde{\mu}_{3,3}$ parameter fitted to 106.38(53) mD. For the modelling of the whole rotational spectrum, a set of *ab initio* effective dipole moment parameters was also derived for the first time. The value of the *ab initio* effective parameter $\tilde{\mu}_{3,3}^{ab\,initio}$ of 117.8 mD is in good agreement with the fitted value. The *ab initio* line list shows that CF$_4$ rotational transitions belonging to other vibrational states will be accessible in other spectral ranges with the actual degree of sensitivity of the CRDS-THz setup. For example, the ν_3–$2\nu_4$ vibrational state transitions will be accessible at THz frequencies using an AMC covering higher frequencies with a pair of photonic mirrors of suitable dimensions. Nevertheless, the transitions belonging to other fundamental states such as GS–GS or $\nu_4 - \nu_4$ are too weak to be measured with this setup, and a sensitivity improvement of several orders is required for their observation. The improvement of cavity stability by its thermal management will allow a higher degree of accumulation to be undertaken.

Conflicts of interest

There are no conflicts to declare.

Acknowledgements

Notes and references

1 V. Boudon, J.-P. Champion, T. Gabard, G. Pierre, M. Loëte and C. Wenger, *Environ. Chem. Lett.*, 2003, **1**, 86–91.

12356 | *Phys. Chem. Chem. Phys.*, 2024, **26**, 12345–12357

This journal is © the Owner Societies 2024

2 C. M. Trudinger, P. J. Fraser, D. M. Etheridge, W. T. Sturges, M. K. Vollmer, M. Rigby, P. Martinerie, J. Mühle, D. R. Worton, P. B. Krummel, L. Paul Steele, B. R. Miller, J. Laube, F. S. Mani, P. J. Rayner, C. M. Harth, E. Witrant, T. Blunier, J. Schwander, S. O'Doherty and M. Battle, *Atmos. Chem. Phys.*, 2016, **16**, 11733–11754.

3 H. De Longueville, L. Clarisse, S. Whitburn, C. Clerbaux, G. Lecomte and P. Coheur, *J. Quant. Spectrosc. Radiat. Transfer*, 2023, **311**, 108755.

4 M. Carlos, O. Gruson, C. Richard, V. Boudon, M. Rotger, X. Thomas, C. Maul, C. Sydow, A. Domanskaya, R. Georges, P. Soulard, O. Pirali, M. Goubet, P. Asselin and T. Huet, *J. Quant. Spectrosc. Radiat. Transfer*, 2017, **201**, 75–93.

5 V. Boudon, M. Carlos, C. Richard and O. Pirali, *J. Mol. Spectrosc.*, 2018, **348**, 43–46.

6 A. Cuisset, F. Hindle, G. Mouret, R. Bocquet, J. Bruckhuisen, J. Decker, A. Pienkina, C. Bray, E. Fertein and V. Boudon, *Appl. Sci.*, 2021, **11**, 1229.

7 F. Hindle, R. Bocquet, A. Pienkina, A. Cuisset and G. Mouret, *Optica*, 2019, **6**, 1449.

8 C. Elmaleh, F. Simon, J. Decker, J. Dumont, F. Cazier, M. Fourmentin, R. Bocquet, A. Cuisset, G. Mouret and F. Hindle, *Talanta*, 2023, **253**, 124097.

9 M. Rey, I. S. Chizhmakova, A. V. Nikitin and V. G. Tyuterev, *Phys. Chem. Chem. Phys.*, 2018, **20**, 21008–21033.

10 M. Rey, I. S. Chizhmakova, A. V. Nikitin and V. G. Tyuterev, *Phys. Chem. Chem. Phys.*, 2021, **23**, 12115–12126.

11 G. Mouret, M. Guinet, A. Cuisset, L. Croize, S. Eliet, R. Bocquet and F. Hindle, *IEEE Sens. J.*, 2013, **13**, 133–138.

12 J. van Helden, R. Peverall and G. Ritchie, *Cavity Ring-Down Spectroscopy: Techniques and Applications*, Wiley, 2010, pp. 27–56.

13 D. A. Landman, R. Roussel-Dupre and G. Tanigawa, *Astrophys. J.*, 1982, **261**, 732.

14 V. Boudon, M. Carlos, C. Richard and O. Pirali, *J. Mol. Spectrosc.*, 2018, **348**, 43–46.

15 C. Bray, A. Cuisset, F. Hindle, G. Mouret, R. Bocquet and V. Boudon, *J. Quant. Spectrosc. Radiat. Transfer*, 2017, **203**, 349–354.

16 M. R. Aliev and J. K. G. Watson, *Higher-order effects in the vibration-rotation spectra of semirigid molecules*, Academic Press, London, 1985.

17 D. Papousek and M. R. Aliev, *Molecular vibrational-rotational spectra*, Elsevier Scientific Publishing Company, Amsterdam-Oxford-New York, 1982.

18 V. Boudon, J.-P. Champion, T. Gabard, M. Loëte, M. Rotger and C. Wenger, *Handbook of High-Resolution Spectroscopy*, Wiley, Chichester, West Sussex, United Kingdom, 2011, vol. 3, pp. 1437–1460.

19 M. Rey, *J. Chem. Phys.*, 2022, **156**, 224103.

20 C. Wenger, V. Boudon, M. Rotger, J. P. Sanzharov and J. P. Champion, *J. Mol. Spectrosc.*, 2008, **251**, 102–113.

21 M. Takami, *J. Chem. Phys.*, 1980, **73**, 2665–2672.

22 M. Takami, *J. Chem. Phys.*, 1981, **74**, 4276–4285.

23 H. Berger, *J. Phys.*, 1977, **38**, 1371–1375.

24 J. V. Auwera, 2023, Private Communication.

25 I. E. Gordon, L. S. Rothman, R. V. C. Hill, Y. Tan, P. F. Bernath, M. Birk, V. Boudon, A. Campargue, K. V. Chance, B. J. Drouin, J.-M. Flaud, R. R. Gamache, J. T. Hodges, D. Jacquemart, V. I. Perevalov, A. Perrin, K. P. Shine, M.-A. H. Smith, J. Tennyson, G. C. Toon, H. Tran, V. G. Tyuterev, A. Barbe, A. Csaszar, M. V. Devi, T. Furtenbacher, J. J. Harrison, A. Jolly, T. Johnson, T. Karman, I. Kleiner, A. A. Kyuberis, J. Loos, O. M. Lyulin, S. T. Massie, S. N. Mikhailenko, N. Moazzen-Ahmadi, H. S. P. Müller, O. V. Naumenko, A. V. Nikitin, O. L. Polyansky, M. Rey, M. Rotger, S. Sharpe, K. Sung, E. Starikova, S. A. Tashkun, J. V. Auwera, G. Wagner, J. Wilzewski, P. Wcislo, S. Yu and E. J. Zak, *J. Quant. Spectrosc. Radiat. Transfer*, 2017, **203**, 3–69.

26 M. Rey, A. V. Nikitin and V. G. Tyuterev, *Adtrophys. J.*, 2017, **847**, 1.

27 M. Rey, A. V. Nikitin, Y. L. Babikov and V. G. Tyuterev, *J. Mol. Spectrosc.*, 2016, **327**, 138–158.

28 A. Domanskaya, K. Berezkin, G. Li, H. Bohlius, M. Kim, J. Harrison and V. Ebert, *J. Quant. Spectrosc. Radiat. Transf.*, 2023, **311**, 108790.

29 J. K. G. Watson, *Mol. Phys.*, 1968, **15**, 479–490.

30 V. Tyuterev, S. Tashkun, M. Rey and A. Nikitin, *Mol. Phys.*, 2022, **120**, e2096140.

31 J. Van Vleck, *Phys. Rev.*, 1929, **33**, 467.

32 J. P. Champion, M. Loëte and G. Pierre, in *Spherical Top Spectra*, eds K. N. Rao, A. Weber, Academic Press, San Diago, 1992.

33 A. V. Nikitin, J. P. Champion and V. G. Tyuterev, *J. Mol. Spectrosc.*, 1997, **182**, 72–84.

34 V. Boudon, O. Pirali, P. Roy, J.-B. Brubach, L. Manceron and J. Vander Auwera, *J. Quant. Spectrosc. Radiat. Transfer*, 2010, **111**, 1117–1129.

35 M. Rey, A. V. Nikitin and V. G. Tyuterev, *Phys. Chem. Chem. Phys.*, 2013, **15**, 10049–10061.

36 C. Richard, V. Boudon and M. Rotger, *J. Quant. Spectrosc. Radiat. Transfer*, 2020, **251**, 107096.